Adaptive Near-Field Imaging with Robotic Arrays

Belal Korany*, Chitra R. Karanam*, and Yasamin Mostofi
University of California Santa Barbara
Santa Barbara, CA, USA
Email: {belalkorany, ckaranam, ymostofi}@ece.ucsb.edu

***Abstract*—In this paper, we are interested in phased-array imaging of an unknown area using narrowband RF signals and arrays synthesized by an unmanned vehicle. Typical phased array imaging approaches use fixed or pre-determined array configurations for imaging, which are not usually informative for the whole area. In this paper, we then propose an iterative adaptive imaging approach where we identify the uncertain regions in an initial image that need to be sensed better, find the optimal array location and orientation for such a sensing task and finally combine the new image with the initial image to obtain a better overall imaging quality. Such an approach is easily enabled by using robots to synthesize arrays. We validate our proposed approach with numerical simulations and show that an adaptive approach improves the imaging quality as compared to imaging with fixed arrays.**

***Index Terms*—Near-field beamforming, Robotic arrays, Adaptive imaging.**

I. Introduction

Robots and unmanned vehicles are now being used to assist humans in a variety of tasks. For instance, robots are now capable of performing tasks such as imaging an area, localization, enabling connectivity, and distributed sensing and beamforming [1]–[7]. More specifically, using robots for tasks such as imaging and localization with RF signals is of particular interest since they can utilize their mobility to image the objects present in any unknown area, even through walls. In this paper we are interested in imaging an unknown area with narrowband RF signals, utilizing the mobility of robots to synthesize antenna arrays.

Phased-array imaging using RF signals has been extensively explored in the literature. Solutions using MUSIC [8] and beamforming [9], [10] have been proposed for imaging point targets as well as extended targets. However, these solutions required using wideband signals, which might not always be available on small or off-the-shelf devices in order to equip unmanned vehicles with the necessary resources for imaging an area. Therefore, phased-array imaging with narrowband signals (e.g., WiFi, Bluetooth, ZigBee) is a problem of considerable interest, but challenging to solve [11]. Some of the challenges associated with narrowband imaging can be addressed by using methods that utilize arrays with different perspectives or views around an unknown area, in order to generate multiple images that can then be fused together for a better overall image [12]–[14]. However, such methods are not effective when imaging extended targets. Furthermore, all the proposed approaches collect measurements on fixed or pre-determined array configurations. In this paper we propose an adaptive approach, where we find the optimal array in order to image any particular region of interest in the area and thereby improve the overall imaging quality. Robots are particularly useful for such a setting, since they can easily position and synthesize arrays at any desired location around the area.

The rest of the paper is organized as follows. In Section II, we describe the general setup of the near-field imaging problem and the issues associated with a fixed-array approach to imaging with narrowband signals. In Section III, we discuss our proposed iterative approach for adaptive imaging of an unknown area. We then present numerical results in Section IV and conclude in Section V.

This work is funded by NSF CCSS award #1611254.
*Authors contributed equally to this work.

II. Problem Setup

Consider an unknown area $\mathbf{D}$ that we are interested in imaging using narrowband RF signals. $\mathbf{D}$ could contain various objects, whose locations and shapes are completely unknown. Two robots are deployed outside the area $\mathbf{D}$, and they are tasked with imaging the area. One transmitting robot (Tx) transmits RF signals from a fixed position p_{t} and the other robot receives the corresponding scattered signals. We can utilize the mobility of the robots to synthesize antenna arrays as well as position the synthesized arrays at various locations around the area of interest. To synthesize an antenna array of length N, the receiver (Rx) robot moves along a desired linear route to collect measurements of the received scattered signal magnitude and phase, at Rx positions $q_r, \mathrm{r} = 1, \ldots, N$. Then, the measured scattered field at the Rx positions can be used to image the area by using Near-field beamforming principles to focus on each point in the area [15]. More specifically, we can form the image $I(x)$ at any location x in the area as

$$I(x) = \left| \sum_{r=1}^{N} R(q_r) e^{j \frac{2\pi}{\lambda} \left(\|x - p_{\mathrm{t}}\|_2 + \|x - q_r\|_2 \right)} \right|, \qquad (1)$$

where $\|.\|_2$ is the l_2-norm of the argument, and $R(q_r)$ is the received scattered signal at the Rx at position q_r normalized to have unit magnitude [16].

The response of the imaging system (the image formed by the array) when focusing on a point target in the area is called the Point Spread Function (PSF). When using narrowband signals for imaging, the corresponding PSF spreads out in different directions locally around the point of focus. Fig. 1 (a) shows an example PSF for imaging using an Rx array on the left side of the workspace, for a frequency of operation

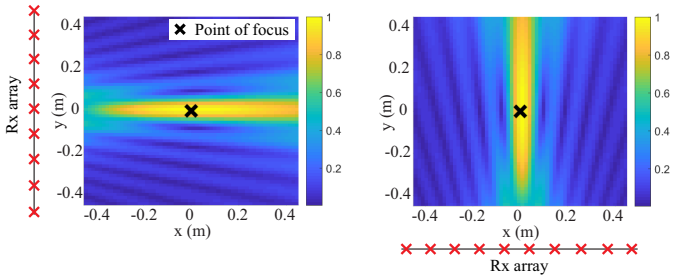

(a) (b)

Fig. 1. Point spread functions of arrays with different locations and orientations focusing on the same point.

5.18 GHz. This PSF spreading causes the value of $I(x)$ at x to depend on the presence of x within the PSFs at other locations which have an object. This gives rise to *ghost* objects in the image, which are pixels of relatively high intensity at locations in $I(x)$ which did not contain any objects.

Since different arrays with different locations and orientations result in vastly different PSFs for the same point of focus, multi-array image fusion is one of the techniques proposed in the literature to improve the image quality [12]–[14]. Images from different arrays will all contain peaks at the same point of focus but will have different spreading patterns, as shown in Fig. 1. Hence, simple multiplicative image fusion will peak at the target point and suppress the ghost regions [16]. However, multiplicative image fusion is suitable only for point targets. In the case of extended targets, multiplicative fusion will only image the illuminated part of the target, giving no information about the target size or shape. Instead, illuminating the area from multiple views/perspectives and using additive fusion captures the shape and/or size of the object, albeit not solving the previously mentioned ghost objects problem. In the next section, we then propose an adaptive approach that iteratively increases the imaging quality by sensing the ghost regions with an array that corresponds to the optimal PSF for that region.

III. Adaptive Imaging Approach

In this section, we describe our proposed iterative approach for adaptive imaging of an area by using a robot to synthesize an antenna array at a desired location and orientation. As discussed in the previous section, PSFs from different arrays have different shapes and spreading patterns. Hence, the image of a specific region in the workspace might be affected by the objects if imaged from one array, but not affected when imaged from another array with a different location and orientation. We propose to take advantage of this property and utilize the mobility of robots to synthesize different arrays that can then be used with the desired PSFs to image any particular region in the unknown area.

Fig. 2 shows an overall outline of our proposed adaptive imaging framework, which consists of three main components: (a) obtaining the initial image, (b) finding regions which contain objects and regions of uncertainty in the image, and (c) finding the optimal array which can sense and image the uncertain regions to decrease their uncertainty. We next describe each of these components in detail.

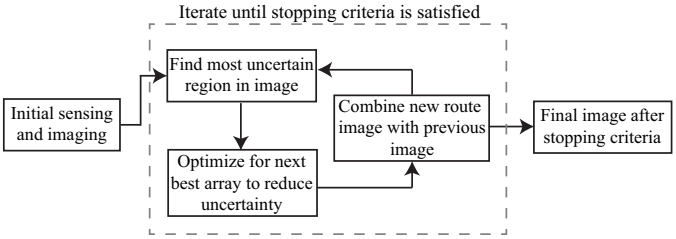

Fig. 2. Block diagram of the proposed adaptive imaging framework.

A. Initial Sensing and Imaging

We first obtain an initial image of the area by adding images from several arrays around the area, as described in Section II. This initial image can be obtained using any configuration of the arrays. In this paper, we propose to obtain the initial scattering data using four linear arrays of the Rx robot on the four sides of the workspace, with the Tx robot always located in front of the center of the corresponding receiver array. As discussed previously, the PSF at any point in the area has a spread around that point. Therefore, the PSFs corresponding to the object locations corrupt the image intensity value at pixels which are inside the spread of these PSFs. Consequently, the initial image is not usually completely informative of all the objects, and could have various ghost targets or uncertain regions (as we shall see in Sec. IV).

B. Finding an Uncertain Region

Given the initial image, we are next interested in finding the regions in the area that need to be sensed better, so that we have a better idea of the presence or absence of objects at every location in the unknown area $\mathbf{D}$. More specifically, we are interested in segmenting the previously obtained initial image into regions that correspond to objects (with a high probability) and regions of uncertainty. Here, we define uncertain regions as those pixels whose intensity in the image is not high enough to certainly be an object, and is not low enough to declare the absence of an object.

Regions with high probability of object presence: We first threshold the previously obtained initial image to define regions that correspond to the presence of objects (with a high probability). We use the method described in [12] to calculate this threshold, denoted by γ_{th}. This method aims at maximizing the detection probability given a certain probability of false alarm. More specifically, if we denote the null hypothesis by H_0 (the event of no object at pixel x), then γ_{th} is calculated such that the probability of false alarm at x is maintained to a certain value p_{FA}, i.e. $P(I(x) = y \geq \gamma_{\text{th}}|H_0) = p_{\text{FA}}$. This can be calculated by generating multiple training scenarios with objects present at various locations in the area and observing the Probability Density Functions (PDF) of the intensities of pixels with no objects ($P(I(x) = y|H_0)$). We then use this threshold γ_{th} in the initial image and detect the pixels corresponding to the presence of an object as those pixels with intensities above γ_{th}. We then form convex regions corresponding to these object pixels and label these regions as the objects in the area. More specifically, we fit circles with

the smallest radius that can enclose any group of co-located object pixels, and label these circles as the object regions. We use a binary mask $\mathbf{O}(x)$ to denote the object regions, where $\mathbf{O}(x) = 1$ if x is inside any of the circles, and 0 otherwise.

Region with highest uncertainty: Next, we are interested in finding the most uncertain region in the remaining parts of the image. As described previously, an uncertain region is that which has an intensity that is not high enough to certainly correspond to an object, but is not low enough to correspond to the absence of an object. In order to detect such a region of high uncertainty in the image, we first calculate a mean uncertainty intensity γ_{u} such that $\gamma_{\text{u}} = E\left[I(x) = y < \gamma_{\text{th}} | H_1\right]$, where H_1 is the event of an object being present at the pixel x, from the previously generated training scenarios. This captures the mid-range value of the intensities that can be confused for either the presence or absence of an object (H_1 or H_0). We then generate superpixels in the remaining part of the image (where the intensity is less than γ_{th}), which are perceptually meaningful atomic regions that are similar in intensity values [17]. We finally select the most uncertain region as the superpixel whose average intensity is closest to γ_{u}. We denote this region by a mask $\mathbf{U}(x) = 1$ if the pixel x is inside the highest uncertain superpixel, and 0 otherwise.

C. Optimization Framework for Next Best Route

Given the uncertain region $\mathbf{U}$ that we need to sense better, we are next interested in finding the optimal location and orientation of an array that would be able to reduce the uncertainty in $\mathbf{U}$. The image obtained using such an array should ideally be such that the intensities of pixels in the uncertainty region are not affected by other objects in the area. To this end, we examine the PSF of a linear array focusing on a point along the perpendicular bisector of the array, as shown in Fig. 1. We can see that the PSF is concentrated inside a *cone* whose width is $\propto \frac{\lambda S}{L}$, where L is the array length and S is the distance away from the array [18]. Furthermore, the PSF decays outside that cone. We also make the following observations:

- Ideally, if the uncertainty region $\mathbf{U}$ falls inside that cone, and the object regions $\mathbf{O}$ are far outside the cone, then the objects will not affect this array's imaging quality for $\mathbf{U}$.
- If the objects are closer to the array than the uncertain region $\mathbf{U}$, then the scattered signal from these objects would outpower the scattered signals from any possible objects in the uncertain region under test. Hence, objects are preferred to be further away from the array than the uncertain region.

To mathematically characterize these preferences, we model the PSF using a PSF mask $\mathbf{P}(x) \propto \frac{1}{D(x)\psi(x)}$, where $D(x)$ is the distance between the pixel x and the center of the array, and $\psi(x)$ is the angle between the line connecting x to the center of the array and the perpendicular bisector of the array. We are then interested in finding an optimal array, that maximizes the overlap of its PSF mask $\mathbf{P}(x)$ with the region $\mathbf{U}(x)$, while simultaneously minimizing its overlap with the object regions $\mathbf{O}(x)$. Regarding the possible space of array locations and orientations, we consider arrays whose centers can be located at any angle θ on a circle of radius R that encompasses the area $\mathbf{D}$, and that can be oriented towards any direction ϕ with respect to the x-axis. It is evident that each possible PSF mask $\mathbf{P}(x)$ is a function of θ and ϕ. Therefore, the optimization problem that we are interested in solving can be posed as follows:

$$\begin{aligned} \{\theta^*, \phi^*\} = \underset{\theta,\phi}{\text{argmax}} \quad & \sum_x \mathbf{P}_{\theta,\phi}(x)(\mathbf{U}(x) - \alpha \mathbf{O}(x)) \\ \text{subject to} \quad & 0 \leq \theta < 2\pi, \;\; 0 \leq \phi < \pi, \end{aligned} \tag{2}$$

where α is a regularization parameter that can be tuned to give more weight to either avoiding object regions or including the uncertain regions within the PSF mask. The solution for the optimization problem depends on the choice of $\mathbf{P}_{\theta,\phi}$. However, since the optimization is over only two finite-space variables, we can exhaustively search over the entire space of the variables for any $\mathbf{P}_{\theta,\phi}$, and find the θ^* and ϕ^* that correspond to the optimal array for sensing $\mathbf{U}$.

We then set the robot to collect measurements along the new array and generate an image of the area $I_{\mathbf{U}}(x)$ using Eq. 1 on only the new measurements. However, we obtained $I_{\mathbf{U}}(x)$ using an array optimized for region $\mathbf{U}$. Therefore, we combine $I_{\mathbf{U}}(x)$ with the initial input image $I(x)$ as

$$I_{\text{final}}(x) = W_{\mathbf{U}}(x) I_{\mathbf{U}}(x) + (1 - W_{\mathbf{U}}(x)) I(x), \tag{3}$$

where $W_{\mathbf{U}}(x) \in [0, 1]$ is any smooth mask that gives more weight to $I_{\mathbf{U}}(x)$ inside the region $\mathbf{U}$ and less weight outside.

Finally, the combined image is again used as an initial image in the pipeline, in order to find the next most uncertain region in the image, and a corresponding optimal array. The stopping criteria for the iterations depend on the amount of resources available for sensing (e.g., time or motion energy constraints), since the quality of the image only improves with every iteration.[1] Thus, using our proposed framework, we obtain a final image that clearly indicates the presence and absence of objects in the area as compared to the initial image.

IV. Numerical Results

In this section, we provide MATLAB simulation results for our proposed adaptive imaging approach using robotic arrays. In these simulations, the initial image is formed using arrays of length 1 m, and $\lambda/2$ antenna spacing, located 0.5 m away from each side of the workspace, with the Tx of each array located 10 cm in front of the array. We also use $p_{\text{FA}} = 0.01$ and $\alpha = \sum_x \frac{2\mathbf{U}(\mathbf{x})}{\mathbf{O}(\mathbf{x})}$. Fig. 3 shows the results of the proposed pipeline for the area with two square objects shown in Fig. 3 (a). The received scattered signals were calculated using the method in [19]. The individual images are then formed by the four arrays on all four sides of the area and additively fused together to generate the initial image shown in Fig. 3 (b). We can see that this plot captures the locations of the objects, as evident from the detected object regions $\mathbf{O}$. However, it is still not completely informative about the area

[1]Note that every optimized array reduces the uncertainty in the image at each iteration, therefore additional iterations would not add any uncertainty.

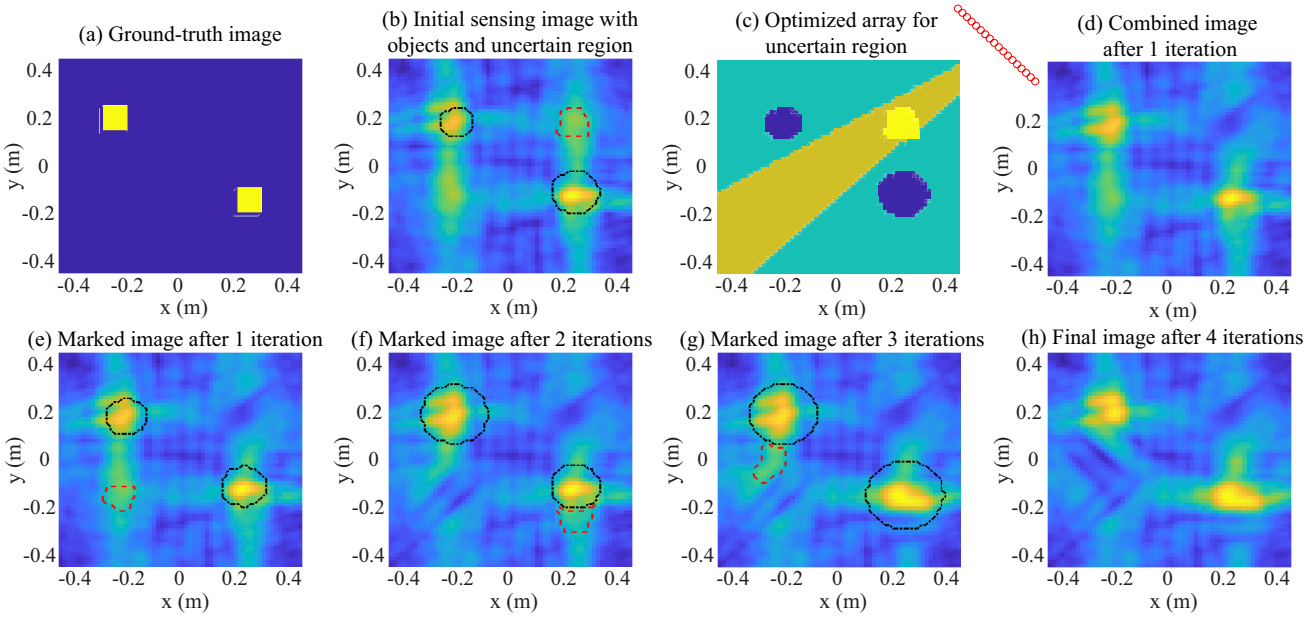

Fig. 3. Imaging result for the two-object scenario. (a) shows the ground truth image, (b) shows the initial image obtained from additive fusion of arrays on four sides of the area, (c) shows location and orientation of the optimized array to image the uncertain region (yellow area) avoiding the object regions (blue areas), (d) shows the combined image that has lower intensity in the uncertain region, (e)-(h) are outputs of successive iterations in the algorithm, with each iteration reducing the uncertainty of the uncertain region of the image of the previous iteration. In all plots, black dot-dash lines represent the object region boundaries, while red dashed lines denote the uncertain region boundary.

since it has *ghost* regions where the intensities of the pixels are moderately high. The location of the most uncertain superpixel (the uncertain region $\mathbf{U}$) calculated by our approach is also shown on the plot. Fig. 3 (c) then shows the result of the optimization step, where the optimal array for imaging $\mathbf{U}$ was found. It is evident from the figure that the main *cone* of this array covers the uncertain region $\mathbf{U}$ entirely while avoiding the object regions $\mathbf{O}$. We then collect measurements on this optimized array and generate the image for the whole area $I_{\mathbf{U}}$, which is combined with the initial image of Fig. 3 (b) as described in Sec. III-C to obtain the combined image shown in Fig. 3 (d). As mentioned in Sec. III-C, $W_{\mathbf{U}}$ could be any mask of choice, which gives more weight to $I_{\mathbf{U}}$ within the uncertain region $\mathbf{U}$. For this example, we chose $W_{\mathbf{U}}$ such that

$$W_{\mathbf{U}}(x) = \begin{cases} 0.55 + 0.45\cos\left(\frac{\pi d'(x)}{2R'}\right) & \text{if } d'(x) \leq 2R', \\ 0.1 & \text{if } d'(x) > 2R', \end{cases} \quad (4)$$

where $d'(x)$ is the distance between point x and the centroid of $\mathbf{U}$, R' is the smallest radius of a circle containing $\mathbf{U}$. We can see that the intensity values of $\mathbf{U}$ decreased, and accordingly, the region became more certain. Next, Fig. 3 (e)—(h) show the output images of more iterations of the algorithm on the same example. It can be seen that each iteration clears out uncertainties in the $\mathbf{U}$ region of its input image, thereby increasing the quality of the overall image over time. Finally, we provide another example scenario to show the performance of our proposed approach. Fig. 4 (a) shows the initial image of a scene with three square objects whose boundaries are marked in black dashed lines. Fig. 4 (b) shows the final image after 4 iterations of our proposed algorithms. The figure shows enhancement in the quality of the image by reducing the intensities of ghost regions and emphasizing the object regions.

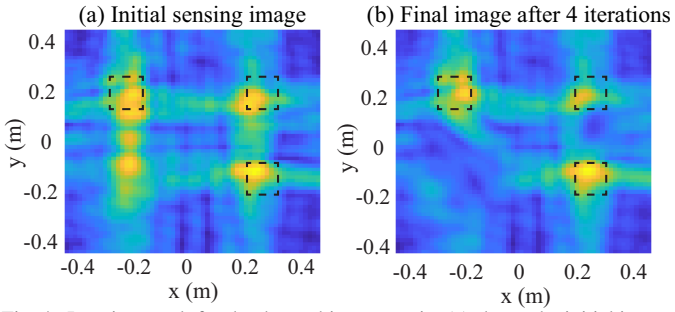

Fig. 4. Imaging result for the three-object scenario. (a) shows the initial image and (b) shows the final image obtained after 4 iterations using our proposed approach. We can see that while the initial image had ghost objects, the final image suppresses the ghost objects and captures the true objects. The black dashed lines depict the ground-truth objects.

V. Conclusions

In this paper, we considered the problem of imaging an unknown area using narrowband signals and robotic arrays. We proposed an adaptive imaging approach that utilizes the mobility of the robots to take advantage of the diversity of images obtained from arrays with different perspectives. Our framework iteratively identifies object regions and uncertain regions in an input image of the area, and then optimally designs antenna arrays that produce a clear image of the uncertain regions. We have validated our framework through numerical simulations for multiple scenarios, and showed an enhancement of the quality of the images by suppressing the ghost objects and emphasizing the true objects.

REFERENCES

[1] S. Depatla, L. Buckland, and Y. Mostofi, "X-ray vision with only WiFi power measurements using Rytov wave models," *IEEE Transactions on Vehicular Technology*, vol. 64, no. 4, pp. 1376–1387, 2015.

[2] C. R. Karanam and Y. Mostofi, "3D through-wall imaging with unmanned aerial vehicles using WiFi," in *2017 16th ACM/IEEE International Conference on Information Processing in Sensor Networks (IPSN)*. IEEE, 2017, pp. 131–142.

[3] C. R. Karanam, B. Korany, and Y. Mostofi, "Magnitude-Based Angle-of-Arrival Estimation, Localization, and Target Tracking," in *Proceedings of ACM/IEEE International Conference on Information Processing in Sensor Networks*, April 2018, pp. 254–265.

[4] J. Djugash, S. Singh, G. Kantor, and W. Zhang, "Range-only SLAM for robots operating cooperatively with sensor networks," in *Proceedings of IEEE International Conference on Robotics and Automation (ICRA)*. IEEE, 2006, pp. 2078–2084.

[5] P. N. Pathirana, N. Bulusu, A. V. Savkin, and S. Jha, "Node localization using mobile robots in delay-tolerant sensor networks," *IEEE transactions on Mobile Computing*, vol. 4, no. 3, pp. 285–296, 2005.

[6] Y. Yan and Y. Mostofi, "Robotic router formation in realistic communication environments," *IEEE Transactions on Robotics*, vol. 28, no. 4, pp. 810–827, July 2012.

[7] A. Muralidharan and Y. Mostofi, "Energy optimal distributed beamforming using unmanned vehicles," *IEEE Transactions on Control of Network Systems*, 2017.

[8] F. Foroozan and P. Sadeghi, "Super-resolution ultrawideband ultrasound imaging using focused frequency time reversal MUSIC," in *2015 IEEE International Conference onAcoustics, Speech and Signal Processing (ICASSP)*. IEEE, 2015, pp. 887–891.

[9] Y.-S. Yoon and M. G. Amin, "Imaging of behind the wall targets using wideband beamforming with compressive sensing," in *IEEE/SP 15th Workshop on Statistical Signal Processing, 2009.* IEEE, 2009, pp. 93–96.

[10] F. Ahmad, M. G. Amin, and S. A. Kassam, "Synthetic aperture beamformer for imaging through a dielectric wall," *IEEE transactions on aerospace and electronic systems*, vol. 41, no. 1, pp. 271–283, 2005.

[11] D. Huang, R. Nandakumar, and S. Gollakota, "Feasibility and limits of WiFi imaging," in *Proceedings of the 12th ACM Conference on Embedded Network Sensor Systems*. ACM, 2014, pp. 266–279.

[12] C. Debes, M. G. Amin, and A. M. Zoubir, "Target detection in single- and multiple-view through-the-wall radar imaging," *IEEE Transactions on Geoscience and Remote Sensing*, vol. 47, no. 5, pp. 1349–1361, 2009.

[13] C. Le, T. Dogaru, L. Nguyen, and M. A. Ressler, "Ultrawideband (UWB) radar imaging of building interior: Measurements and predictions," *IEEE Transactions on Geoscience and Remote Sensing*, vol. 47, no. 5, pp. 1409–1420, 2009.

[14] C. H. Seng, A. Bouzerdoum, M. G. Amin, and S. L. Phung, "Two-stage fuzzy fusion with applications to through-the-wall radar imaging," *IEEE Geoscience and Remote Sensing Letters*, vol. 10, no. 4, pp. 687–691, 2013.

[15] A. J. Devaney, "Time reversal imaging of obscured targets from multistatic data," *IEEE Transactions on Antennas and Propagation*, vol. 53, no. 5, pp. 1600–1610, 2005.

[16] G. Gennarelli and F. Soldovieri, "Multipath ghosts in radar imaging: Physical insight and mitigation strategies," *IEEE Journal of Selected Topics in Applied Earth Observations and Remote Sensing*, vol. 8, no. 3, pp. 1078–1086, 2015.

[17] R. Achanta, A. Shaji, K. Smith, A. Lucchi, P. Fua, and S. Süsstrunk, "SLIC superpixels compared to state-of-the-art superpixel methods," *IEEE transactions on pattern analysis and machine intelligence*, vol. 34, no. 11, pp. 2274–2282, 2012.

[18] M. M. Goodwin and G. W. Elko, "Constant beamwidth beamforming," in *IEEE International Conference on Acoustics, Speech, and Signal Processing (ICASSP), 1993*, vol. 1. IEEE, 1993, pp. 169–172.

[19] D. E. Livesay and K. M. Chen, "Electromagnetic fields induced inside arbitrarily shaped biological bodies," *IEEE Transactions on Microwave Theory and Techniques*, vol. 22, no. 12, pp. 1273–1280, 1974.